Experimental Deconvolution of Resistance Contributions in Commercial Solid Oxide Cells with Ni-CGO Electrode

Hagen, Anke; Padinjarethil, Aiswarya Krishnakumar; Heijne, Jelle

Published in:
Electrochimica Acta

Link to article, DOI:
10.1016/j.electacta.2023.142672

Publication date:
2023

Document Version
Publisher's PDF, also known as Version of record

Electrochimica Acta 461 (2023) 142672

Contents lists available at ScienceDirect

Electrochimica Acta

journal homepage: www.journals.elsevier.com/electrochimica-acta

Experimental deconvolution of resistance contributions in commercial solid oxide cells with Ni-CGO electrode

Anke Hagen [a,*], Aiswarya Krishnakumar Padinjarethil [a,b], Jelle Heijne [a,c]

[a] DTU Energy, Technical University of Denmark, Fysikvej B. 310, Kongens Lyngby 2800, Denmark
[b] Topsoe A/S, Haldor Topsøes Allé 1, 2800 Kongens Lyngby, Denmark
[c] Energy Technology Group, Department of Mechanical Engineering, Eindhoven University of Technology, NPS Driven. De Hammen 1, MK Ravenstein 5371, Netherlands

ARTICLE INFO

Keywords:
Solid oxide cell
Ni-CGO electrode
Electrochemical impedance spectroscopy
Deconvolution

ABSTRACT

Solid oxide cells (SOCs) convert the energy of a fuel to electrical energy (fuel cell mode) and electrical energy into a fuel such as hydrogen (electrolysis mode) with exceptionally high efficiencies (>60% and >90%, respectively). They are flexible in terms of usable fuels & gasses and operating modes such as dynamic and reversible. Therefore, SOCs can be a solution for the intermittent nature of renewable energy sources, which are increasingly implemented in modern energy systems. Among state-of-the-art (SoA) SOCs, electrolyte supported cell (ESC) configurations are in the process of commercialization. They are typically composed of Ni-CGO fuel electrodes, YSZ electrolytes, and an LSCF-CGO air electrode. Key to optimize performance and durability is the detailed knowledge of how the cell components contribute to the total cell resistance, typically obtained through electrochemical impedance analysis. This is a challenge for SoA ESCs, because all the electrode contributions overlap strongly at the low frequency ranges below and around ca. 1 Hz. The present study succeeded with experimentally de-convoluting the different electrode contributions. The approach was to carry out impedance studies on two versions of ESC, one SoA with Ni-CGO and LSCF-CGO electrodes and one with Ni-CGO and LSM-YSZ electrodes, where the frequencies of the air electrode contributions are separated from the fuel electrode contributions.

1. Introduction

Solid oxide cells (SOCs) are energy conversion devices with high efficiencies and flexibility. SOCs can operate in both modes –fuel cell and electrolysis – and can thus contribute either to electricity production, to electricity storage, to power-to-X solutions or to balancing purposes through reversible operation. They are fuel flexible and can operate on hydrogen fuel and alternative hydrogen carriers such as biogas, e-gas or ammonia in fuel cell mode and on steam plus carbon dioxide in electrolysis mode yielding a synthesis gas (CO and hydrogen). Most mature SOC generations use Ni-YSZ (Nickel - Yttria stabilized Zirconia) or Ni-CGO (Nickel - Gadolinia doped Ceria) cermet as the fuel electrode, YSZ as electrolyte, and LSCF (lanthanum strontium cobaltite ferrite) or LSC (lanthanum strontium cobaltite) based air electrodes [1–3].

Identification and quantification of the contributions of electrode processes to the overall cell resistance has been a key for understanding performance and degradation in detail. It has also been essential for developing next generation, improved cells. The most applied tool to attain this knowledge is electrochemical impedance spectroscopy (EIS), where different loss mechanisms express themselves as responses at different frequencies. Through comprehensive studies, frequency ranges for losses like gas transport, electrode reactions etc. have been determined (see a list with the corresponding references in Table 1). On the basis of these studies, the EIS was de-convoluted for most common SOCs. The experimental approach for such deconvolution is to vary one experimental parameter while keeping all others constant and to record EIS. For example, the oxygen partial pressure in the gas at the air electrode is varied (e.g., air vs. oxygen) in order to identify air electrode processes, or the steam partial pressure (e.g., dry hydrogen, wet hydrogen) or carbon content (methane/steam, CO/steam) at the fuel electrode in order to identify fuel electrode processes. Furthermore, variation of the temperature distinguishes thermally activated processes with different activation energies and processes of different nature such as electrochemical and gas transport processes (e.g., Barfod et al. [4]).

For fuel electrode supported cells with Ni-YSZ fuel electrodes and

* Corresponding author.
E-mail address: anke@dtu.dk (A. Hagen).

https://doi.org/10.1016/j.electacta.2023.142672
Received 9 March 2023; Received in revised form 10 May 2023; Accepted 28 May 2023
Available online 29 May 2023

Table 1
List of typical EIS frequency regions at 750–850 °C and their assignment to SOC losses on fuel electrode supported SOC with Ni-YSZ fuel electrodes.

f/Hz	Loss mechanism	Conditions	Reference
1–4	Gas conversion	Ni-YSZ	[4,7,8]
20–50	Gas diffusion	Ni-YSZ	[7,8]
20–200	Electrode polarization	LSC*/LSC-CGO	[8,9,10,5]
100–1000	Electrode polarization	LSCF, LSCF-CGO	[8,6,11]
1100	Dissociative adsorption of O_2 and transport to triple phase boundary (TPB)	LSM-YSZ	[4,7]
1000–10,000	Charge transfer between Ni and YSZ and diffusion of charged species to the TPB	Ni-YSZ	[4,7,8]
50,000–62,000	Transport of O-intermediates at LSM-YSZ interface	LSM-YSZ	[4,7]

* Metal supported cell configuration, 650 °C.

LSM-YSZ air electrodes (LSM: lanthanum strontium manganite), frequency regions for each electrode contribution, gas conversion and transport are well-separated in the EIS at temperatures around 750 °C and below (e.g., [4]).

When the LSM-YSZ air electrode is substituted by mixed ionic electronic conducting (MIEC) materials such as LSCF or LSC, the EIS deconvolution becomes more difficult because the frequency region representing the air electrode processes moves towards lower values and start to overlap with other low frequency processes [5,6]. The typical frequency ranges determined for Ni-YSZ fuel electrode supported cells with LSM-YSZ or LSCF and LCO based air electrodes are listed in Table 1. Frequency ranges are dependent on temperature. As this study deals with ESC, the focus here is on the temperatures of ca. 750–850 °C. Not all processes are relevant for all cell concepts. For example, while diffusion contributions are typically seen on Ni-YSZ in a fuel electrode supported configurations, they are negligible or absent in electrolyte supported cells (ESCs), due to the thin fuel electrode layer.

An additional challenge appears when Ni-CGO instead of Ni-YSZ fuel electrodes are considered. Processes at this electrode move from intermediate towards low frequencies (from kHz ranges to 3–10 Hz, e.g., [12]), where they overlap with both, gas transport and air electrode processes as well (see Table 1). In addition, the variation of the degree of doping in CGO and the change of the oxidation state of Ce results in a range of activation energies, making evaluation of temperature dependencies very complex [13–17]. The toolbox with variation of gas compositions as mentioned above does no longer allow for a deconvolution of EIS. An alternative approach is to study the Ni-CGO contributions separately in symmetric cell configurations or on model electrodes/cells (for example [16]). However, the nature of the electrolyte/electrode interface or microstructure of full cells cannot always be matched completely by those configurations, leading to deviations of frequency ranges or magnitudes of resistance contributions. In addition, one of the - equal in materials - electrodes acts as anode and the other as cathode, which can give differences compared to a fuel, commercial cell with two different electrode materials. Furthermore, tests of symmetric cells or model electrodes/cells are often carried out under conditions not completely matching full cell or stack environment, such as gas flow configurations, single atmospheres, smaller dimensions etc. Thus, the direct transfer of EIS data to full cells is not always possible.

In order to overcome these limitations, the present study made use of another approach. The LSCF-CGO air electrode in the electrolyte supported cell configuration was substituted by an LSM-YSZ electrode, which is known to contribute to the EIS at high frequencies (see Table 1) and thus well separated from the Ni-CGO contributions, while the Ni-CGO to YSZ electrolyte interface was identical to the full cell in question, because the same half-cells were used. Thus, the current study employed full cells with Ni-CGO fuel electrodes and either LSCF-CGO or LSM-YSZ air electrodes, in order to determine experimentally the Ni-CGO contribution in electrolyte supported cell configuration. The test setup for full cells is optimized to mimic the cell conditions in a full stack as good as possible in order to be able to directly transfer the results to real applications. This gives the best testing environment for gaining the relevant knowledge, i.e., frequency ranges, electrode resistances, and activation energies. An EIS study on these two full cells was carried out by varying gas compositions to the electrodes and temperature.

2. Experimental

2.1. Cell configurations

The two cell configurations in this study are illustrated in Fig. 1.

The LSCF-ESC (Fig. 1a) was provided by Sunfire. It consists of a Ni-CGO fuel electrode functional layer (15–20 µm) with a ca. 2 µm CGO layer close to the dense 3YSZ electrolyte (3 mol% yttria stabilized zirconia, 80–85 µm), a CGO barrier layer and an LSCF-CGO air electrode (30–35 µm), and finally an LSMC (lanthanum strontium manganite cobaltite) contact layer (ca. 5 µm). The LSM-ESC (see Fig. 1b) was fabricated starting from a commercial half-cell with the same layers and thicknesses as described above. Instead of the LSCF-CGO electrode, an LSM-YSZ air electrode (LSM25, TZ8Y, 25–30 µm) was screen printed and sintered at 930 °C for 24 h Afterwards, an LSM contact layer was screen printed. These cells were tested with a size of 5.3 × 5.3 cm^2 and an active area of 16 cm^2.

2.2. Cell test setup

The full cells were tested in dual atmosphere test rigs. Geometries for cell fixture and gas flows are optimized to reflect the situation of a cell in a stack. The ESC was placed in an alumina house in a sandwich configuration with gas distribution and contact layers.

Gold seal was used on the fuel side and Ni and gold current collectors were used as the contact layer in the form of a coarse and fine meshes for the fuel and air side, respectively. To ensure good contact on the Ni side, the meshes were corrugated and an extra height of 0.6 mm was provided depending on the cell configurations. Weights were added to achieve good sealing and electrical contact to the cell. There was no seal on the air side; the cell outlet gas was directed to the furnace. More details are provided in ref. [18]. The data acquisition was automated using an in-house software ('DTU Energy RFCcontrol').

2.3. Test protocol

The full cells were firstly reduced at 850 °C according to manufacturer's protocol. They were heated up to 850 °C in Argon and reduced under safety gas (diluted hydrogen: 5% vol H_2 in N_2) for 2 h, followed by pure H_2 for 1 h. The cells were then characterized under different gas compositions as well as different temperatures. The conditions used for the present study are summarized in Table 2. The cells were characterized with EIS at open circuit voltage (OCV). Impedance spectra were recorded using a Solartron Frequency Analyzer. EIS was recorded from 96.5 kHz to 0.01 Hz with an AC current perturbation of amplitude 0.06

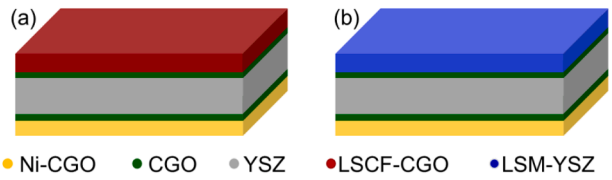

Fig. 1. Illustration of electrolyte supported cell configurations used in this study, a) Ni-CGO/CGO/YSZ/CGO/LSCF-CGO electrolyte supported full cell (denoted LSCF-ESC) and b) Ni-CGO/CGO/YSZ/CGO/LSM-YSZ electrolyte supported full cell (denoted LSM-ESC).

Table 2
Test conditions for the characterization of full cells.

T/ °C	Fuel electrode gas H_2/H_2O/mol/mol	Air electrode gas O_2/mol
850, 800, 750	96/4, 80/20, 50/50	0.21 (air), 1 (O_2)

A and with 12 points per decade.

2.4. Data analysis

Evaluation of EIS was carried out using Nyquist and Bode plots and a number of simple mathematical treatments of the real (*Zreal*) and imaginary (*Zimag*) part and the frequency. Specifically, (i) the difference of the imaginary part (Delta *Zimag*) vs. frequency, (ii) the first derivative of the real part (*Zreal*) of the relevant impedance spectrum according to Eq. (1), which averages five points (data *f*), and (iii) Complex Nonlinear Least Square (CNLS) fit were employed. CNLS fitting was carried out using ZView.

$$\frac{\partial Zreal}{\partial lnf} = \frac{Zreal_{(f-2)} - Zreal_{(f+2)}}{\ln(f-2) - \ln(f+2)} \quad (1)$$

Activation energies (E_A) were determined using the Arrhenius plot of the natural logarithm of the respective polarization resistance *Rp* vs. T^{-1} in K, deriving the energy value from the slope of the linear trend, using the gas constant *R* in $J{\cdot}K^{-1}{\cdot}mol^{-1}$ according to Eq. (2), where *A* is the pre-exponential factor.

$$\ln(Rp) = \ln(A) - \frac{E_A}{RT} \quad (2)$$

3. Results and discussion

3.1. Identification of resistance contributions

The overall objective was to identify and quantify the losses in an ESC with Ni-CGO fuel electrode and LSCF-CGO air electrode. Fig. 2 shows the EIS of the commercial LSCF-ESC while varying the steam content in hydrogen at the fuel electrode and the oxygen partial pressure at the air electrode. The plots reveal the sensitivity of the EIS towards steam content in hydrogen; the polarization resistance decreases as the degree of humidity increases, as expected (e.g., [19]) (Fig. 2a). This effect is clearly observed in the Bode plot, where the serial resistance is not seen (Fig. 2b) and the delta Bode plot (Fig. 2c), with the affected frequency around 0.2 Hz. This response at low frequencies is a direct result of material specific properties of CGO, which is known to have a large surface capacitance leading to a response at the lower frequencies. Grosselindemann et al. [16] and Nakamura et al. [20] observed a steam dependency on the peak below ca. 1 Hz as well, measured on symmetric cells. The large dependency on the steam partial pressure points to enhanced kinetics. This frequency peak was therefore correlated to a surface process, potentially a charge transfer process [16]. Furthermore, a very small middle frequency contribution at ca. 10 Hz is observed, which is overlapping with the low frequency peak and becomes only visible in the difference plot because it is slightly affected by the steam partial pressure (see Fig. 2c). Similar observations were reported by Grosselindemann et al. [16] and the origin related to a bulk process, specifically, the oxide ion transport in the MIEC bulk of Ni-CGO.

The dependence of the resistance on the partial oxygen pressure in the air electrode is only minor, most probably due to the high activity of the MIEC air electrode material. The Nyquist plots are nearly superimposed when recording the EIS in air or oxygen at the air electrode (Fig. 2a, blue and dark green data). This result is confirmed using the Bode plot (see Fig. 2b) and in the delta Bode plot showing that the difference is close to zero over the whole frequency range (Fig. 2c). The LSCF-CGO electrode processes are thus not significantly limited by the partial gas pressures in the investigated range. This result can be explained by the fast kinetics at this electrode; therefore the significant changes appear only at lower p_{O2} values (<0.21 bar) [11], which were not applied in this study. The Bode plot (Fig. 2b) discloses furthermore, that all loss contributions appear in the low frequency region below ca. 2 Hz, underlining the challenge for approaching any deconvolution of electrode contributions in cells with Ni-CGO electrodes as discussed in the introduction.

To be able to distinguish between fuel and air electrode contributions in a full cell with an identical fuel electrode to electrolyte interface and an identical Ni-CGO electrode microstructure, an ESC with an alternative air electrode was studied. Any impact of different interfaces (for example from symmetric cell studies) or test environment when using smaller cell pieces or different test setups can be avoided with this approach.

Fig. 3 shows the EIS for the cell with an LSM-YSZ air electrode (and Ni-CGO fuel electrode). In comparison with the LSCF-ESC, the ohmic resistance is significantly higher (compare Fig. 3a to Fig. 2a). Furthermore, also the polarization resistance is larger, although not to such significant extent as the ohmic resistance. In contrast to LSCF, LSM is not a mixed ionic electronic conductor, i.e., ion conduction is only happening through the YSZ phase and electron conduction through the LSM phase in the composite electrode. Current constrictions in a not-optimized electrode can occur and increase the ohmic resistance. It has to be noted that the LSM-YSZ air electrode in this study was not optimized as it is an experimental tool, and the only function was to shift the air electrode contributions to a frequency region clearly separated from the Ni-CGO fuel electrode. Thus, the larger ohmic resistance seen in Fig. 3a can be attributed to several factors such as the lower conductivity of LSM [7], a potentially worse contact to the barrier layer (CGO on the electrolyte), or not optimized composite structure/thickness of the

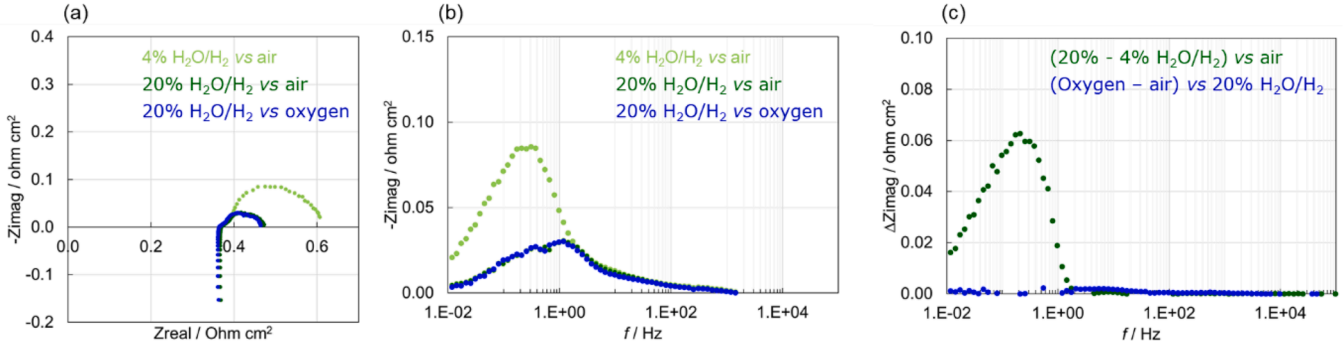

Fig. 2. LSCF-ESC: Nyquist (a), Bode (b), and delta Bode (c) plots recorded under 4% H_2O in H_2 (light green markers), 20% H_2O in H_2 at the fuel electrode and air at the air electrode (dark green markers), 20% H_2O in H_2 with oxygen at the air electrode (blue markers). The delta plot shows the difference between 4% and 20% H_2O in H_2 vs. air at the air electrode (green marker), and between air and oxygen vs. 20% H_2O in H_2 (blue marker), 850 °C.

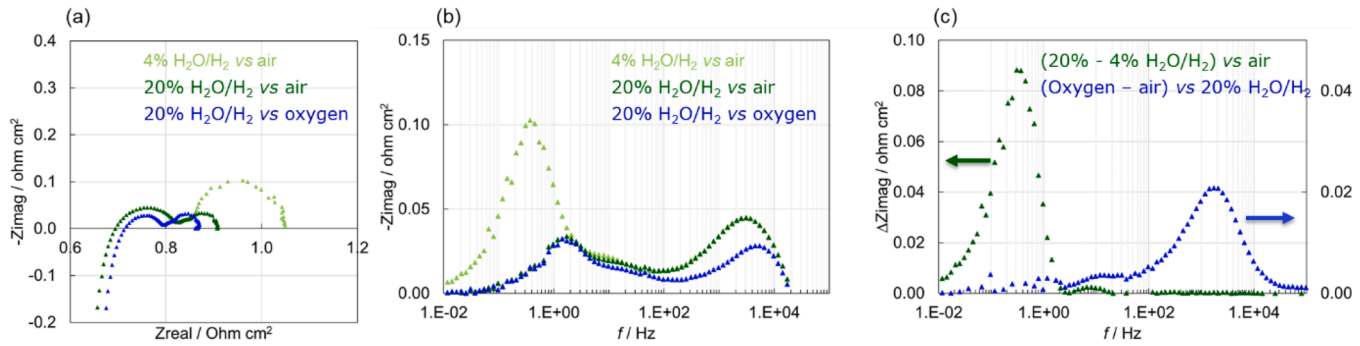

Fig. 3. LSM-ESC: Nyquist (a), Bode (b), and delta Bode (c) plots recorded under 4% H_2O in H_2 (light green markers), 20% H_2O in H_2 (dark green markers) at the fuel electrode and air at the air electrode, 20% H_2O in H_2 with oxygen at the air electrode (blue markers). The delta plot shows the difference between 4% H_2O and 20% H_2O in H_2 vs. air at the air electrode (green marker), and between air and oxygen vs. 20% H_2O in H_2 (blue marker), 850 °C.

electrode. In addition, there is an effect of the air electrode gas on the ohmic resistance. This might be due to the not optimized interface between LSM-YSZ on top of the CGO layer and the microstructure within the LSM-YSZ layer. It is known, that imperfect microstructures in these electrodes can lead to decreased conductivity in the electrode, for example due to restrictions around larger particles & imperfect composite mixture [4]. Whether the LSM-YSZ electrode has a good or bad microstructure and performance should not affect the aim of the study, i.e., the nature of the contributions and frequency positions. The larger polarization resistance can be explained in terms of the lower electrochemical activity of LSM-YSZ compared to LSCF-CGO, which is a MIEC electrode (both LSCF as well as CGO show mixed ionic and electronic conductivity) with higher conductivity and more available reaction sites. The Bode plot of the LSM-ESC (Fig. 3b) reveals a contribution at a frequency of 4000 Hz, which was not observed in the LSCF-ESC.

When increasing the steam content in hydrogen, the impedance decreases (Fig. 3a, green EIS) as expected [7] and as already seen on the LSCF-ESC (see Fig. 2a). The affected frequencies are identical with the one observed on the LSCF-ESC under the same conditions (see Figs. 3b, c and b, c). The middle frequency contribution appears more significant when looking at the effect of steam (Fig. 3c). The two cells with the different air electrodes thus exhibit identical behavior of the (same) Ni-CGO fuel electrode.

Substituting air at the air electrode by oxygen causes changes in the impedance at a frequency region of ca. 4000 Hz as seen in the Bode plot (dark green and blue markers, Fig. 3b) and even more pronounced in the delta Bode plot (blue markers in Fig. 3c). This is a clear indication of this process being related to the air electrode, also when comparing to literature results (e.g., [4,9]). Therefore, the EIS proves that the frequency contributions of the air electrode indeed shift towards higher frequencies, away from the Ni-CGO fuel electrode contributions, which was the actual goal of substituting the air electrode material in the ESC. In addition, there is an effect of the air electrode gas on a contribution at middle frequency, ca. 10 Hz (see Fig. 3c). It seems that the middle frequency response is affected by both, the fuel and the air electrode gas. Regarding the effect related to the air electrode in the LSM-ESC, the frequency range indicates a diffusion process. It can be related to the not optimized porous structure in this electrode. On the other hand, the low frequency peak (ca. 1 Hz, see Figs. 2b and 3b) can clearly be assigned to the Ni-CGO fuel electrode and can be quantified.

Several options have been used to distinguish better – resolve – the contributions from the electrodes and electrode processes based on EIS, such as distribution of relaxation times (DRT, e.g., [6]), Analysis of Differences in Impedance Spectra (ADIS, e.g., [21,22]) or Differential Impedance Analysis (DIA, e.g., [23]). In this study, the first derivative of the real part of the EIS was used for a detailed analysis on the LSCF-ESC and LSM-ESC with the aim to determine the frequency ranges for the electrode contributions. Such analysis uses elements of ADIS and DIA, without taking differences of different spectra (ADIS) or establishing equivalent circuit elements used in the case of DIA. ADIS was not applied because the aim was to identify summit frequencies at each specific condition, while ADIS would yield intermediate frequency values through the subtraction of spectra recorded in different gas mixtures. The approach used here makes direct use of experimental data avoiding complex mathematical manipulations (like in DRT), which can lead to the appearance of artefacts, for example when EIS is carried out on non-model cells, such as the commercial cells in this study. The effect of gas compositions on the EIS contributions are plotted in Fig. 4. Comparison of Fig. 4a and b highlights the effect of 4% or 20% steam content in hydrogen at the fuel electrode and comparison of Fig. 4b and c highlights the effects of air or oxygen at the air electrode for the two cells: LSCF-ESC and LSM-ESC. The observed frequencies, their

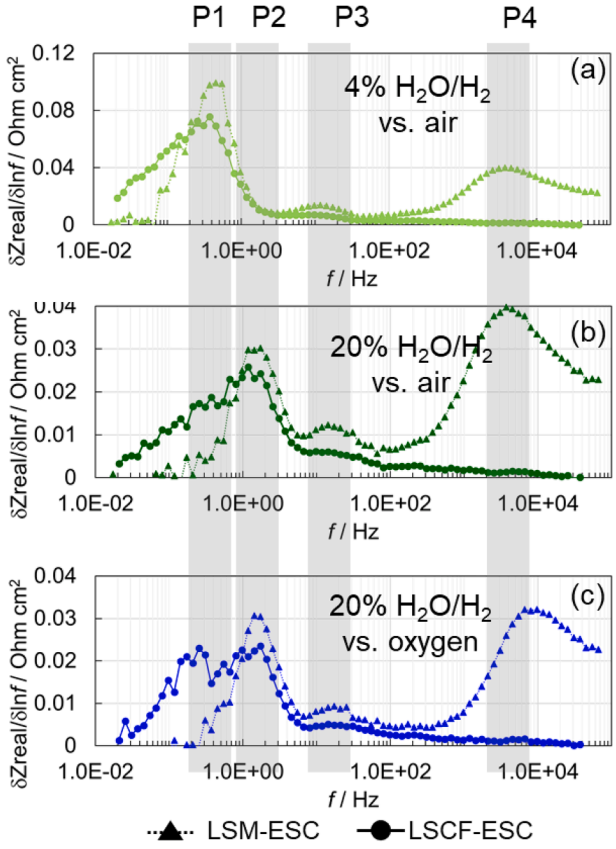

Fig. 4. *Zreal* derivative plots of LSM-ESC (triangle, stippled line) and LSCF-ESC (circle, solid line) at 850 °C, in 4% steam in hydrogen vs. air at the air electrode (a), 20% steam in hydrogen vs. air at the air electrode (b), and 20% steam in hydrogen vs. oxygen at the air electrode (c).

dependency on gas compositions, and assignments are summarized in Table 3.

In summary, four contributions can be distinguished for the cells. A first peak or rather shoulder (P1) occurs at 0.3 Hz (in oxygen at the air electrode). It is only visible on the LSCF-ESC and it is affected by the air electrode atmosphere. When using oxygen instead of air, the frequency shifts to lower values and therefore it is somewhat separated as peak from the following, bigger one (Fig. 4c). However, due to the noise in the measured data, this effect appears to be very weak. The noise level and small magnitude of the effect might explain, why there was no significant difference in the spectra when plotting the difference of the Bode spectra (see Fig. 2c). The position, appearance and gas dependency indicate the LSCF air electrode as source for this contribution. A main peak (P2) occurs at ca. 1 Hz on both cells. When decreasing the steam content in the hydrogen fuel, this peak increases significantly in magnitude (see Fig. 4a and b, note that the y-axis scale in Fig. 4a is larger as compared to Fig. 4b and c) and the frequency shifts to lower values. The large dependency on the steam concentration, in particular when going from rather dry to wet conditions, and the appearance on both cells points clearly to the Ni-CGO fuel electrode. The frequency shift towards lower values also leads to more overlap with the contributions from the LSFC air electrode, when recording EIS in hydrogen fuel gas with low degree of humidity, making a meaningful deconvolution of the two contributions based on such EIS impossible. Furthermore, the result that P1, arising from the LSCF contribution, is rather a shoulder compared to the major peak P2 related to the Ni-CGO electrode underlines that the Ni-CGO impedance is dominating and can overshadow the LSCF air electrode impedance.

There is a minor contribution in the middle frequency range (P3, ca. 10 Hz), which is observed for both cells and has actually a minor dependence on both the gas compositions at the air and the fuel electrode. Grosselindemann et al. [16] observed a contribution in the same frequency range in a symmetrical cell with LSCF electrode. The authors attribute this contribution to a diffusion because of the week dependency on the temperature. A significant fourth peak (P4) at high frequency (ca. 4 kHz) only occurs for the LSM-ESC. It is very sensitive to the air electrode gas composition (see Fig. 4b and c), where the summit frequency shifts to higher values of ca. 8 kHz when using oxygen instead of air, and the magnitude decreases. Such a decrease of resistance in oxygen was previously reported for the LSM-YSZ air electrode in Ni-YSZ supported cells [24]. This is a clear indication that this high frequency contribution is related to LSM-YSZ air electrode processes. Previous EIS studies on cells with LSM-YSZ air electrodes in a fuel electrode supported configuration revealed a frequency contribution around 1100 Hz at 850 °C [4,7]. The loss was ascribed dissociative adsorption of O_2 and transport to the TPB. The position in the present study is in line with those studies, in particular as the fuel gas composition does not affect the peak. The difference of the specific summit frequency value in this work could be related to the additional CGO layer between electrolyte and LSM-YSZ electrode in this work.

While varying the gas compositions at the electrodes gives information about the effect of partial pressures on electrode reactions, variation of the temperature provides information about thermally activated contributions. Because recording EIS on the LSM-ESC resolves fuel from air electrode contributions by shifting the latter towards higher frequencies, results on this cell are discussed for activation energies. As the interest is on electrode responses, the ohmic resistance is not considered; it of course increases with decreasing temperature. The EIS plot as function of temperature is shown in Fig. 5. The green curve is the same as in Fig. 4b (for the LSM-ESC), only the scale of the y-axis is different.

There is no shoulder at the position P1 (see Table 3), because the cell does not contain an LSCF-CGO air electrode. The contributions with summit frequencies at 1 Hz (P2) and at 4500 Hz (P4) change with changes of the temperature. The low frequency contribution assigned to Ni-CGO shifts to slightly higher and the high frequency contribution assigned to LSM-YSZ shifts to lower frequencies with decrease of temperature. These opposite trends might be due to the nature of their origins. The CGO might be sensitive to the temperature in relation to changes in its capacitance, which may result in this slight shift to lower frequencies, whereas for LSM, the related process should be thermally activated, thus resulting in the shift to higher frequencies. Both impedances increase in magnitude with decreasing the temperature, the LSM-YSZ related one to a significantly larger extent, which points to a charge transfer process. The contribution at ca. 10 Hz (P3) seems not significantly affected, neither the summit frequency nor magnitude. This indicates a diffusion impedance as main origin, at least under the given conditions.

3.2. Quantification of resistance contributions

The results of this EIS analysis provided input for identifying and applying an equivalent circuit model. The aim was to quantify the Ni-CGO electrode contribution based on the results of the LSM-ESC, where air and fuel electrode contributions are separated as discussed above. The equivalent circuit used for CNLS fitting is shown in Fig. 6. It consists of an inductance, an ohmic resistance, which is the contribution arising primarily from the dense electrolyte, and the three polarization losses for the LSM-ESC identified before (see Table 3), i.e. a high frequency LSM-YSZ (P4, constant phase element), a mid-frequency LSM-YSZ diffusion (P3, Warburg element), and a low frequency Ni-CGO (P2, constant phase element) contribution.

The effect of electrode gasses on the obtained resistance contributions are shown in Fig. 7. The Ni-CGO fuel electrode resistance depends on the steam content in the hydrogen fuel and changes in particular when going from very dry conditions (4% steam) to higher steam contents (see yellow columns in Fig. 7). Changes at the air electrode from air to oxygen do not affect the resistance on the other, the fuel electrode (unless there is a gas crossover due to leaks or pinholes in the cells). The middle frequency contribution (here called “Mix”) seems invariant to changes of electrode gasses in terms of magnitude of resistance. On the other hand, the LSM-YSZ air electrode resistance decreases when

Table 3
Polarization contributions at 850 °C determined from plots in Fig. 4, the frequency values are for a 20/80 H_2O/H_2 fuel mixture and air to the air electrode.

No.	*f*/Hz	Cell configuration	Gas dependence	Assignment
1	0.3–0.4	LSCF-ESC	Air electrode gas p_{O2}	LSCF-CGO air electrode
2	2	LSCF-ESC LSM-ESC	Fuel gas humidity	Charge transfer Ni-CGO
3	10–20	LSCF-ESC LSM-ESC	Minor air electrode gas p_{O2} & fuel gas humidity	Ni-CGO bulk process, LSM-YSZ, LSCF-CGO diffusion
4	4500	LSM-ESC	Air electrode gas p_{O2}	LSM-YSZ air electrode

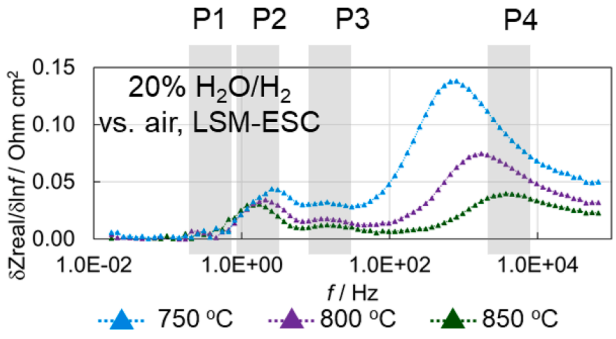

Fig. 5. *Zreal* derivative plots of LSM-ESC in 20% steam in hydrogen vs. air at the air electrode at 750, 800, and 850 °C.

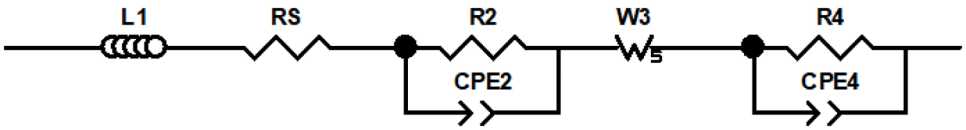

Fig. 6. Equivalent circuit model for the LSM-ESC with Ni-CGO fuel electrode and LSM-YSZ air electrode. The numbering of the electrode contributions follows Table 3.

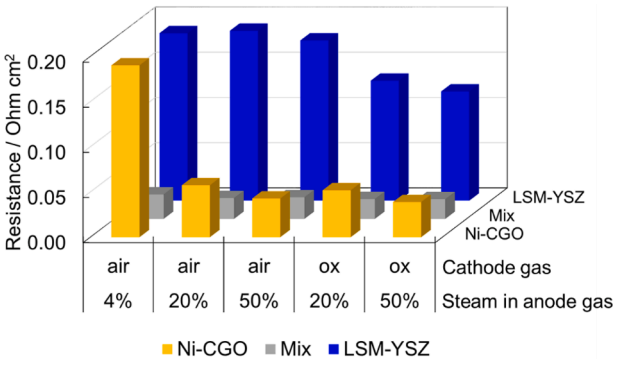

Fig. 7. Resistance contributions of cell components and processes of the LSM-ESC determined via CNLS fitting, data for 850 °C, with air or oxygen (ox) at the air electrode and 4%, 20% or 50% H_2O in hydrogen at the fuel electrode.

changing the respective electrode gas from air to oxygen. This observation is consistent with previous results on symmetric cells and full cells containing LSM-YSZ ([4,7]).

The effect of temperature on electrode contributions was evaluated using the Arrhenius correlation (Eq. (2)). Plots were created; they are shown for the results at 20% steam in hydrogen in Fig. 8. The values deduced from the slope of the linear trend lines are listed in Table 4 for results in 4%, 20%, and 50% steam in hydrogen fuel, together with values from the literature.

Looking at the Ni-CGO electrode, there is a large range of activation energies reported in the literature (ca. 50 to 100 kJ·mol^{-1}, see Table 4). It has to be noted that they were measured with symmetric cell and/or button cell configuration. Furthermore, Iwanschitz et al. [13] and Grosselindemann et al. [16] determined different activation energies for the lower and the higher operating temperatures. According to these studies, a change of energies appeared in the relevant temperature range of the present study, close to 850 °C. The large range of values reflects the variation due to different degrees of Gd doping and microstructural differences. Furthermore, the Ce oxidation state (Ce^{3+}/Ce^{4+}) depends on operating conditions such as temperature range and humidity and can thus vary, also when other than the full, commercial cell

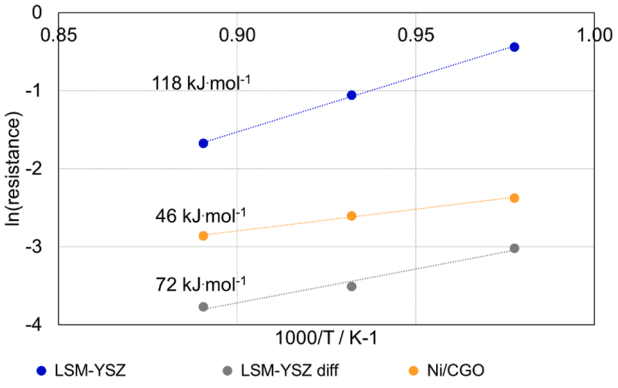

Fig. 8. Arrhenius plot of the LSM-ESC fit results from CNLS fitting using the equivalent circuit in Fig. 6, values from 20% H_2O in H_2 at the fuel electrode and air at the air electrode.

Table 4
Activation energies on the LSM-ESC, deduced from CNLS fitting, and literature values for comparison.

Assignment	Condition	E_A/kJ·mol^{-1}	
	H_2O/H_2/air electrode gas	This study	Literature
Ni-CGO	20/80/air	46	Ca. 50 to 100 [13, 16]
	50/50/air	49	
	20/80/oxygen	48	
	50/50/oxygen	59	
Mix	20/80/air	72	
	50/50/air	7	
	20/80/oxygen	0	
	50/50/oxygen	0	
LSM-YSZ air electrode	20/80/air	118	100–200 [25]
	50/50/air	118	116–125 [7]
	20/80/oxygen	131	
	50/50/oxygen	133	

configurations are examined. The observed significant variation of values depending on specific sample, geometries of test setup and conditions underlines the difficulty to deduce universally applicable values for cells with Ni-CGO electrodes and the need of determining activation energies for the specific cell and conditions in question.

The obtained activation energy for Ni-CGO in this study is in the reported range. It is also consistent with the values reported in the literature for Gd doping within the range used in this work (10–40%) [13]. The Ni-CGO activation energy is only mildly dependent on the degree of humidity in gas in the range between 20 and 50% steam in hydrogen; it increases slightly. At the other extreme, i.e., dry conditions of 4% steam in hydrogen, there are indications of very small activations energies (in the range of 2 kJ mol^{-1}), i.e., following the trend of decreasing activation energies when decreasing the humidity in the fuel. This finding can be explained by the already mentioned dependency of the Ni-CGO response on the Ce^{3+}/Ce^{4+} ratio, which is affected by the degree of humidity, in particular when spanning from very dry to humid conditions. However, CNLS fitting for the spectra as function of the temperature was less robust for the data obtained under dry conditions and the exact value might differ.

Table 4 shows that the activation energies for the LSM-YSZ electrode are very similar to values reported in the literature. Activation energies are the same when determined in fuel gas compositions with different degrees of humidity, which is expected as the air electrode conditions were kept constant. The activation energy is slightly smaller when determined in air vs. oxygen at the air electrode. Obviously, the mechanisms at this electrode are sensitive to the gas composition in the tested range, which was also observed in previous studies by Barfod et al. [4].

The activation energy of the middle frequency "Mix" contribution is significantly dependent on the gas composition at both electrodes (see Table 4). The value of 72 kJ mol^{-1} (see Table 4) in 20/80 steam/hydrogen seems rather high for a diffusion process, which supports the already speculated additional contributions from the fuel electrode bulk process that is more or less dominating depending on the gas composition. The value of 7 kJ mol^{-1} in 50/50 steam/hydrogen corresponds more a diffusion (see Table 4). When leading 100% oxygen to the electrode, the activation energy actually goes to zero independent on the gas composition at the fuel electrode; presumably diffusion limitations at the air electrode disappear under these conditions.

4. Conclusions

The overall objective of the study was to identify and quantify electrode resistance contributions in commercial electrolyte supported cells with Ni-CGO fuel electrode and LSCF-CGO air electrode. The contributions of these electrodes overlap heavily in the EIS, where they appear in the low frequency region below ca. 2 Hz at 850 °C. This makes a deconvolution of the contributions and a quantification using equivalent circuits and CNLS fitting impossible. The variation of gas compositions at the electrodes or the temperature does not remedy this problem. As the behavior of the Ni-CGO electrode is very sensitive towards testing conditions such as gas flow/atmosphere, temperature range, interface structures etc., any results obtained on other items than the specific cell in question in a representative setup can deviate from the commercial cells under real conditions. In order to solve these challenges and to avoid introducing such deviations, a cell with the same fuel electrode and electrolyte (commercial half-cell), but a different air electrode – LSM-YSZ - was fabricated. The identification of the electrode contributions was verified by changes of the gas compositions at the fuel and the air electrodes. Accordingly, the Ni-CGO charge transfer resistance appears at ca. 1 Hz, while the air electrode contributions were observed at ca. 0.3 Hz for the LSCF-CGO and at ca. 4000 Hz for the LSM-YSZ at 850 °C, i.e., clearly separated from the Ni-CGO fuel electrode contribution. As the LSM-YSZ electrode was not optimized, a small diffusion contribution appeared at ca. 10–20 Hz. Further, the Ni-CGO electrode was found to contribute to a small extent with a process in this frequency range.

Based on this assignment and identification of electrode contributions, an equivalent circuit with three electrode contributions was constructed for the cell with Ni-CGO fuel and LSM-YSZ air electrode. Activation energies were determined to ca. 46–59 and 118–133 $kJ{\cdot}mol^{-1}$ for the charge transfer at Ni-CGO and LSM-YSZ, respectively, depending on the gas compositions to the electrodes: 20% and 50% steam in hydrogen at the fuel electrode and air or oxygen at the air electrode. The activation energy of the Ni-CGO contribution was found to be sensitive to the degree of humidity in the fuel gas and of the LSM-YSZ electrode to the oxygen content in the air electrode gas.

The approach of separating the Ni-CGO contribution experimentally from the LSCF-CGO by introducing an alternative air electrode – here LSM-YSZ – into the electrolyte supported cell proved to be successful providing the relevant data for the full, commercial cell, under the desired operating conditions.

CRediT authorship contribution statement

Anke Hagen: Project administration, Funding acquisition, Supervision, Conceptualization, Investigation, Methodology, Resources, Visualization, Writing – original draft. **Aiswarya Krishnakumar Padinjarethil:** Methodology, Investigation, Validation, Visualization, Conceptualization, Data curation, Writing – review & editing. **Jelle Heijne:** Investigation, Methodology, Validation, Visualization, Conceptualization, Data curation, Writing – review & editing.

Declaration of Competing Interest

The authors declare that they have no known competing financial interests or personal relationships that could have appeared to influence the work reported in this paper.

Acknowledgment

The authors gratefully acknowledge the technical support of Henrik Henriksen. This work was supported by the Fuel Cells and Hydrogen Joint Undertaking under Grant Agreement number 825027, AD ASTRA. This Joint Undertaking receives support from the European Union's Horizon 2020 research and innovation program and Hydrogen Europe.

References

[1] D. Udomsilp, C. Lenser, O. Guillon, N.H. Menzler, Performance benchmark of planar solid oxide cells based on material development and designs, Energy Technol. 2001062 (2021) 1, https://doi.org/10.1002/ente.202001062.
[2] D. Stolten, R. Can Samsun, N. Garland, Fuel Cells: Data, Facts and Figures, (978-3-527-33240-3), Editors, WILEY-VCH, 2016.
[3] W. Sitte, R. Merkle, High Temperature Electrolysis - from Fundamentals to Applications, Editors, Blackwells, 2022.
[4] R. Barfod, A. Hagen, S. Ramousse, P.V. Hendriksen, M. Mogensen, Break down of losses in thin electrolyte SOFCs, Fuel Cells 6 (2) (2006) 141, https://doi.org/10.1002/fuce.200500113.
[5] J. Hjelm, M. Søgaard, R. Knibbe, A. Hagen, M. Mogensen, Electrochemical characterization of planar anode supported SOFC with strontium-doped lanthanum cobalt oxide cathodes, ECS Trans. 13 (26) (2008) 285.
[6] A. Leonide, V. Sonn, A. Weber, E. Ivers-Tiffée, Evaluation and modeling of the cell resistance in anode-supported solid oxide fuel cells, J. Electrochem. Soc. 155 (1) (2008) B36.
[7] R. Barfod, M. Mogensen, T. Klemensø, A. Hagen, Y.L. Liu, P.V. Hendriksen, Detailed characterization of anode-supported SOFCs by impedance spectroscopy, J. Electrochem. Soc. 154 (4) (2007) B371.
[8] M. Rao, S.H. Jensen, X. Sun, A. Hagen, Unwinding entangled degradation mechanisms in solid oxide electrolysis cells through electrode modifications and impedance analysis, Fuel Cells 19 (4) (2019) 445, https://doi.org/10.1002/fuce.201800166.
[9] A. Hagen, X. Sun, B.R. Sudireddy, Å.H. Persson, Metal supported SOFCs for mobile applications using hydrocarbon fuels, J. Electrochem. Soc. 167 (2020), 104510, https://doi.org/10.1149/1945-7111/ab9b9d.
[10] A. Hagen, R. Caldogno, F. Capotondo, X. Sun, Metal supported electrolysis cells, Energies 15 (6) (2022) 2045. https://www.mdpi.com/1996-1073/15/6/2045.
[11] A. Leonide, Y. Apel, E. Ivers-Tiffée, SOFC modeling and parameter identification by means of impedance spectroscopy, ECS Trans. 19 (20) (2009) 81, https://doi.org/10.1149/1.3247567.
[12] A. Weber, S. Dierickx, N. Russner, E. Ivers-Tiffée, Sulfur poisoning of Ni-based SOFC-anodes – short and long term behavior, ECS Trans. 77 (10) (2017) 141.
[13] B. Iwanschitz, J. Sfeir, A. Mai, M. Schütze, Degradation of SOFC anodes upon redox cycling: a comparison between Ni/YSZ and Ni/CGO, J. Electrochem. Soc. 157 (2) (2010) B269. https://iopscience.iop.org/article/10.1149/1.3271101.
[14] A. Sciazko, Y. Komatsu, T. Shimura, N. Shikazono, Multiscale microstructural evolutions of nickel-gadolinium doped ceria in solid oxide fuel cell anode, J. Power Sources 478 (2020) 228.
[15] C. Grosselindemann, N. Russner, S. Dierickx, A. Weber, Deconvolution of gas diffusion polarization in Ni/gadolinium-doped ceria fuel electrodes, ECS Trans. 103 (1) (2021) 1375. https://iopscience.iop.org/article/10.1149/10301.1375ecst.
[16] C. Grosselindemann, N. Russner, S. Dierickx, F. Wankmüller, A. Weber, Deconvolution of gas diffusion polarization in Ni/gadolinium-doped ceria fuel electrode, J. Electrochem. Soc. 168 (2021), 124506, https://doi.org/10.1149/1945-7111/ac3d02.
[17] M. Riegraf, R. Costa, G. Schiller, K.A. Friedrich, S. Dierickx, A. Weber, Electrochemical impedance analysis of symmetrical Ni/gadolinium-doped ceria (CGO10) electrodes in electrolyte-supported solid oxide cells, J. Electrochem. Soc. 166 (13) (2019) F865.
[18] A. Hagen, X. Sun, B.R. Sudireddy, Å.H. Persson, Metal supported SOFCs for mobile applications using hydrocarbon fuels, J. Electrochem. Soc. 167 (10) (2020), 104510.
[19] A.K. Padinjarethil, F.R. Bianchi, B. Bosio, A. Hagen, Electrochemical characterization and modelling of anode and electrolyte supported solid oxide fuel cells, Front. Energy Res. 9 (2021) 568.
[20] T. Nakamura, T. Kobayashi, K. Yashiro, A. Kaimai, T. Otake, K. Sato, J. Mizusaki, T. Kawada, Electrochemical behaviors of mixed conducting oxide anodes for solid oxide fuel cell, J. Electrochem. Soc. 155 (6) (2008) B563. https://iopscience.iop.org/article/10.1149/1.2901047.
[21] S.H. Jensen, A. Hauch, P.V. Hendriksen, M. Mogensen, N. Bonanos, T. Jacobsen, A method to separate process contributions in impedance spectra by variation of test conditions, J. Electrochem. Soc. 154 (12) (2007) B1325.
[22] X. Sun, M. Chen, Y.L. Liu, P. Hjalmarsson, S. Dalgaard Ebbesen, S.H. Jensen, M. B. Mogensen, P.V. Hendriksen, Durability of solid oxide electrolysis cells for syngas production, J. Electrochem. Soc. 160 (9) (2013) F1074.
[23] D. Vladikova, The technique of the differential impedance analysis, part II. differential impedance analysis, in: Proceedings of the International Workshop "Advanced Techniques for Energy Sources Investigation and Testing" 4 –9 Sept, Sofia, Bulgaria, 2004.
[24] A. Hagen, M. Menon, S. Ramousse, P.H. Larsen, R. Barfod, P.V. Hendriksen, Properties and performance of SOFC cells produced on a pre-pilot plant scale, Fuel Cells 6 (2) (2006) 146.
[25] W.Z. Zhu, S.C. Deevi, A review on the status of anode materials for solid oxide fuel cells, Mater. Sci. Eng. A 362 (1–2) (2003) 228.